Chemical Engineering Journal 380 (2020) 122522

Contents lists available at ScienceDirect

Chemical Engineering Journal

journal homepage: www.elsevier.com/locate/cej

Low-cost Fe–N–C catalyst derived from Fe (III)-chitosan hydrogel to enhance power production in microbial fuel cells

Wulin Yang[a], Xu Wang[a,b], Ruggero Rossi[a], Bruce E. Logan[a,*]

[a] Department of Civil and Environmental Engineering, The Pennsylvania State University, University Park, PA 16802, United States
[b] School of Resource and Environmental Sciences, Hubei International Scientific and Technological Cooperation Base of Sustainable Resource and Energy, Wuhan University, No. 129 Luoyu Road, Wuhan 430079, PR China

HIGHLIGHTS

- Low cost Fe–N–C catalyst derived from Fe(III)-chitosan hydrogel for oxygen reduction.
- The Fe–N–C/AC catalyst had a $4e^-$ pathway for the oxygen reduction reaction.
- The maximum power density of $2.4 \pm 0.1\,W\,m^{-2}$ was 33% higher than the AC control.

GRAPHICAL ABSTRACT

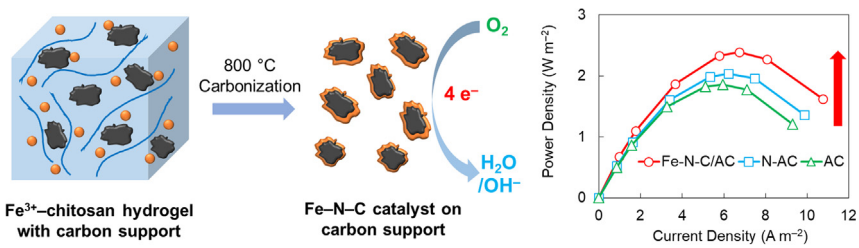

ARTICLE INFO

Keywords:
Fe–N–C
Oxygen reduction reaction
Fe(III)-chitosan hydrogel
Air cathode
Microbial fuel cell

ABSTRACT

A low cost Fe–N–C catalyst on an activated carbon (AC) support was synthesized from inexpensive ferric chloride and chitosan precursors to enhance power production by microbial fuel cells (MFCs). The direct pyrolysis of preformed Fe(III)-chitosan hydrogel as a supporting scaffold created a porous structure on AC with a uniform distribution of Fe active sites. A maximum power density of $2.4 \pm 0.1\,W\,m^{-2}$ was obtained in MFCs using Fe–N–C/AC catalyst, which was 33% higher than the control MFCs using a plain AC catalyst ($1.8 \pm 0.03\,W\,m^{-2}$). The Fe–N–C/AC catalyst was closer to the more efficient four electron transfer pathway for the oxygen reduction reaction (ORR) than the plain AC or chitosan-modified AC. The adoption of chitosan as the N-containing precursor and ferric chloride for the Fe–N–C synthesis added only 6% more in material costs in cathode fabrication, but produced a 33% increase in the maximum power density. This increased power makes the use of this cathode material both economically viable and a sustainable approach to enhance power production in MFCs given the low cost and wide availability of chitosan.

1. Introduction

A microbial fuel cell (MFC) is a sustainable technology to harvest electrical energy from wastewaters [1–6]. In an MFC, the exoelectrogenic bacteria on the anode can degrade organic matter and release electrons that transfer through an external circuit to the cathode, where oxygen in air is usually used as the electron acceptor via the oxygen reduction reaction (ORR) [7–10]. The use of an air cathode, rather than dissolved oxygen in water, avoids the energy intensive aeration process and greatly increases the scalability of MFCs [11–15]. Activated carbon (AC) is currently the most used ORR catalyst in the MFC air cathode due to its low cost of ~$1.4\,kg^{-1}$, compared to a platinum catalyst ($163\,g^{-1}$ for Pt/C, 10% wt) [16]. However, unmodified activated carbon typically catalyzes the ORR via a two electron transfer pathway, which is less efficient compared to the four electron transfer pathway, and thus the use of plain carbon limits power production in MFCs [17].

* Corresponding author.
E-mail address: blogan@psu.edu (B.E. Logan).

https://doi.org/10.1016/j.cej.2019.122522
Received 25 June 2019; Received in revised form 13 August 2019; Accepted 15 August 2019
Available online 17 August 2019
1385-8947/

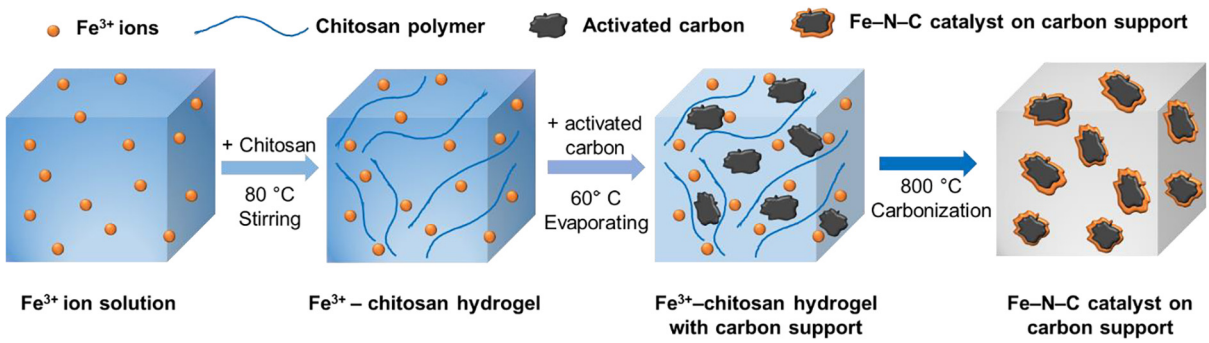

Fig. 1. Synthesis scheme of Fe–N–C catalyst on activated carbon support from Fe(III)–chitosan hydrogel pyrolysis.

Therefore, developing highly active cathode catalysts is essential to improve the power production of MFCs, but these catalyst materials need to be as inexpensive as possible.

Recently, carbon materials containing iron and nitrogen coordination sites (Fe–N–C) have drawn great interest as cathode catalyst in MFCs due to both the high catalytic performance and widely available precursor sources. Fe–N–C catalysts can be easily prepared by direct pyrolysis of Fe–N_x complexes (x = coordination number) or Fe–N based metal organic frameworks under a nitrogen atmosphere [18–20]. For example, an Fe–N–C catalyst derived from ferric chloride and 1,10-phenanthroline immobilized on the AC surface showed 63% higher power production in MFCs than the plain AC catalyst [20]. Other types of N precursors, such as ricobendazole, niclosamide, pyrazinamide, guanosine, sulfacetamide, succinylsulfathiazole, sulfadiazine, and quinine have also been used to synthesize Fe-N-C catalyst for MFCs, and all had a 45% to 55% increase in MFC power compared to the plain AC, with the highest maximum power density of 2 W m^{-2} [19]. Other non-precious metal based materials have also been used as catalysts, such as a 3D templated Fe–N–C catalyst derived from a ferric porphyrin complex that was developed on sacrificial SiO_2 nanospheres [21]. This catalyst had uniformly distributed Fe-N active sites within the porous structure, and a better ORR activity than Pt [21], but making the cathode required a complex fabrication procedure, and the use of a sacrificial support would increase material costs. While the use of these different types of Fe–N–C catalysts has shown good increases in power production in MFCs, the N containing precursors used were all expensive synthetic molecules. Using cathodes with these costly materials and complex preparation procedures could potentially limit fabrication of large MFC cathodes that would be need to be manufactured on order of several hundreds of square meters to make reactors of a scale suitable for commercialized applications [22].

Chitosan is a potentially useful material for cathode fabrication due to its low cost and abundance. Chitosan is the deacetylated derivative of chitin, the second most abundant natural polysaccharide on the planet after cellulose, and it is obtained from crustacean shells, insects, molluscan organs, and fungi [23]. Chitosan has been utilized in many applications as gels, films, or fibers, and particularly as a hydrogel absorbent for environmental contaminants due to its low cost and abundance [24,25]. Chitosan is a copolymer of glucosamine and N-acetylglucosamine, which contains amine functional groups and could function as a nitrogen precursor. Moreover, the amine functional and hydroxyl groups can also complex with different metals such as copper or iron [26,27]. In a recent study, chitosan was used as a nitrogen containing precursor to generate an N and P dual doped cathode catalyst to enhance the performance of MFCs [28]. However, the application of chitosan for the synthesis of Fe–N–C catalyst towards ORR in MFCs has not been previously reported.

In this study, a new and low cost Fe–N–C catalyst on an AC support was facilely synthesized from abundant iron chloride and chitosan precursors by direct pyrolysis of Fe(III)-chitosan hydrogel. The synthesized Fe–N–C catalyst on AC (denoted as Fe–N–C/AC) was benchmarked with AC or solely N doped AC, in terms of both the power production in MFCs and its abiotic electrochemical performance. The physical and chemical properties of the catalysts were further investigated by scanning electron microscope, energy dispersive X-ray spectroscopy, and X-ray photoelectron spectroscopy.

2. Materials and methods

2.1. Materials

Activated carbon (AC) powder (Norit SX plus) was purchased from Norit Americas Inc. Polytetrafluoroethylene (PTFE) of 60% emulsion, chitosan (60% ~ 80% deacetylated), hydrochloric acid (HCl), sodium acetate ($NaC_2O_2H_3$), iron chloride ($FeCl_3$), disodium phosphate (Na_2HPO_4), monosodium orthophosphate ($NaH_2PO_4{\cdot}H_2O$), ammonium chloride (NH_4Cl), potassium chloride (KCl) were purchased from Sigma Aldrich, USA. The hydrophobic polyvinylidene fluoride (PVDF) membrane with pore size of 0.45 μm was purchased from MILLIPORE, USA.

2.2. Catalyst synthesis and cathode fabrication

The Fe–N–C/AC catalyst was synthesized by direct pyrolysis of Fe (III)-chitosan hydrogel (Fig. 1). Anhydrous $FeCl_3$ (1 g) was dissolved and stirred for 10 min in 75 mL of deionized (DI) water. Then, 2 g of chitosan was gradually added into the $FeCl_3$ solution with stirring at 80 °C for 4 h to form the Fe(III)-chitosan hydrogel. AC (6 g) was added into the prepared Fe(III)-chitosan hydrogel and the mixture was stirred for an additional 4 h at 80 °C. The mixture was next transferred to a vacuum oven and dried at 60 °C and 300 torr for 12 h. The dried mixture was heated in a tube furnace (GSL-1700X, MTI Corporation, USA) at 800 °C for 15 min under an N_2 atmosphere, with a 10 °C s^{-1} step increase in temperature. The resulting powder was soaked in 0.01 M hydrochloric acid for 1 h to remove any impurities and washed several times with DI water. The catalyst was dried in the vacuum oven at 60 °C and 300 torr for 6 h. A N–AC catalyst was also synthesized following the same procedure but with only chitosan addition. AC without any modification was used as a control catalyst.

The cathodes were fabricated using a hot pressing method as previously reported [29]. Briefly, a catalyst layer was first fabricated by mixing the prepared catalyst (Fe–N–C/AC, N–AC, or AC) and a 60% PTFE emulsion in ethanol at a AC:PTFE mass ratio of 6:1 with continuous stirring on a hot plate at 60 °C to form a gel. The gel was then pressed at 1×10^7 Pa for 2 s at 60 °C (Model 4388, CARVER, INC., USA), and then folded and pressed again for a total of 3 times. The prepared catalyst layer had a thickness of 780 ± 60 μm with a catalyst loading of 27 ± 1 mg cm^{-2}. The pre-made catalyst layer was then placed between a stainless steel mesh current collector (42 × 42, type 304, McMaster-Carr, USA) and a hydrophobic PVDF membrane diffusion layer, rinsed with ethanol, and then pressed together at 3×10^7 Pa for at least 15 s at 60 °C, and then dried in a fume hood.

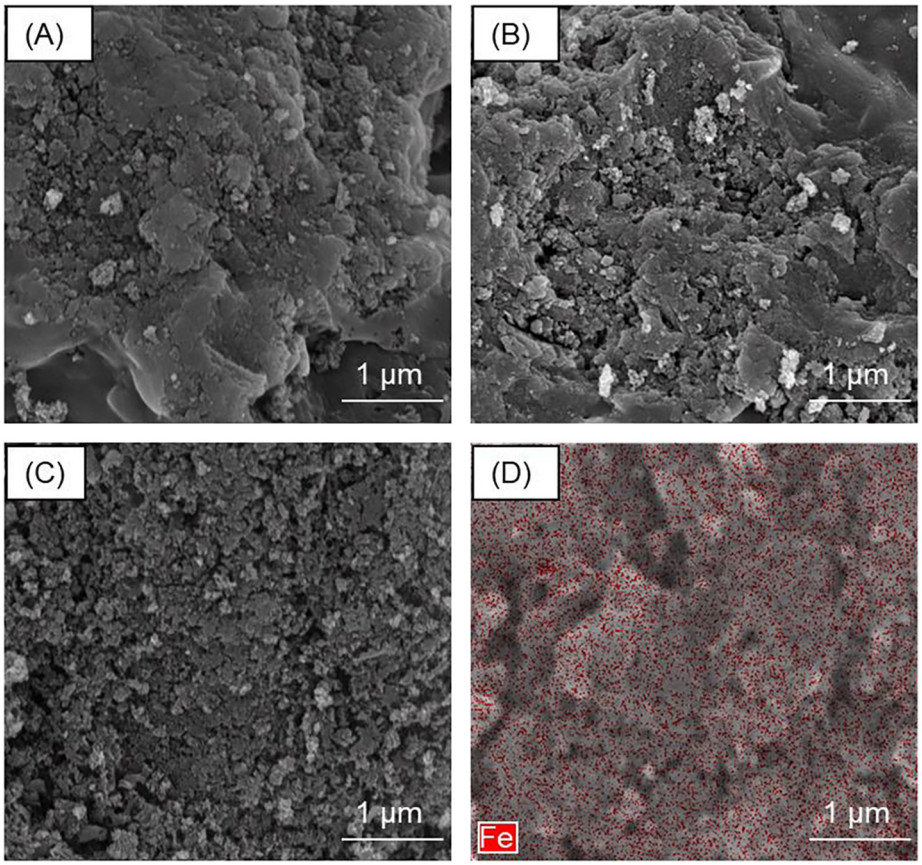

Fig. 2. Surface SEM images of (A) plain AC (B) N–AC (C) Fe–N–C/AC, and (D) EDS mapping of Fe on Fe–N–C/AC with the Fe indicated in red. (For interpretation of the references to colour in this figure legend, the reader is referred to the web version of this article.)

2.3. Surface morphology and characterization

Scanning electron microscopy (SEM; Nova NanoSEM 630, FEI Company, USA) was used to examine the surface morphology of the catalysts. The catalyst powders were dried in an oven at 60 °C for 2 h prior to the analysis. To avoid a charging effect, the catalysts were sputter coated with 10 nm of iridium prior to the SEM imaging. Energy dispersive X-ray spectroscopy (EDS, Silicon Drift Detector-X Max^N, Oxford Instruments, UK) was used to examine the elemental distribution of Fe on Fe–N–C/AC catalyst surface.

X-ray photoelectron spectroscopy (XPS) (Axis Ultra XPS, Kratos Analytical, UK, monochrome AlKα source, 1486 eV) was performed to identify the elemental composition on the catalyst surfaces at a typical sampling depth of 3–6 nm. A quick scan was first conducted to briefly identify characteristic peaks with a high generation energy and short dwell time. High-resolution scans for quantification and chemical state information were collected afterward with a low generation energy and long dwell time. CASA XPS software was used for the elemental and peak fitting analysis.

X-ray diffraction (XRD) analysis was performed in an X-ray diffractometer (XPert Pro MPD, Malvern Panalytical Ltd, UK) with Bragg-Brentano geometry, using Cu K_α (λ = 1.5406 Å) radiation. The phases were compared and identified with the standard powder XRD cards from the Joint Committee on Powder Diffraction Standards (JCPDS).

The Brunauer–Emmet–Teller (BET) surface area and pore volume distribution of catalysts were determined from nitrogen adsorption isotherms at 77.3 K (ASAP 2420, Micromeritics Instrument Corp., GA). The nitrogen absorption data was collected in the relative pressure range of 0.01 to 0.99 and calculated using density functional theory modeling software (MicroActive 2.01). Micropores (< 2 nm), mesopores (2–50 nm) and macropores (> 50 nm) were classified according to the International Union of Pure and Applied Chemistry (IUPAC) definitions [30].

2.4. Preparation of MFC and processing

Single chamber MFCs were constructed from a Lexan block 4 cm in length, with an inside chamber diameter of 3 cm [31]. The anodes were graphite fiber brushes (2.5 cm in both diameter and length) that were heat treated at 450 °C in air for 30 min, and placed horizontally in the middle of MFC chambers, with 1 cm from the brush tip to the cathode. Anodes were fully pre-acclimated by use in MFCs for over one year at a fixed external resistance of 500 Ω, in a constant temperature room (30 °C). The medium used here contained 1 g L^{-1} sodium acetate dissolved in a 50 mM phosphate buffer solution (PBS) (Na_2HPO_4, 4.58 g L^{-1}; $NaH_2PO_4{\cdot}H_2O$, 2.45 g L^{-1}; NH_4Cl, 0.31 g L^{-1}; KCl, 0.13 g L^{-1}; pH = 6.9; κ = 7.29 mS cm^{-1}) amended with 12.5 mL L^{-1} minerals and 5 mL L^{-1} vitamins [32,33]. All the reactors were operated in batch mode.

Single cycle polarization tests were conducted to evaluate the power performance of MFCs, by varying the external resistance from 1000, 500, 200, 100, 75, 50 to 20 Ω at 20 min intervals after initially holding the reactor under open circuit conditions for 2 h. The cathodes were operated in the MFCs for two cycles to stabilize biofilms prior to the polarization tests, with one cycle time of one day. The polarization tests were conducted with duplicate reactors in a constant temperature room at 30 °C [34]. The voltage drop (U) across an external resistor was recorded by a computer based data acquisition system (2700, Keithley Instrument, OH). Current densities (i) and power densities (P) were normalized to the effective projected cathode area (A = 7 cm^2), and calculated as $i = U/RA$ and $P = iU/A$, where R is the external resistance. An Ag/AgCl reference electrode (RE-5B, BASi, West Lafayette,

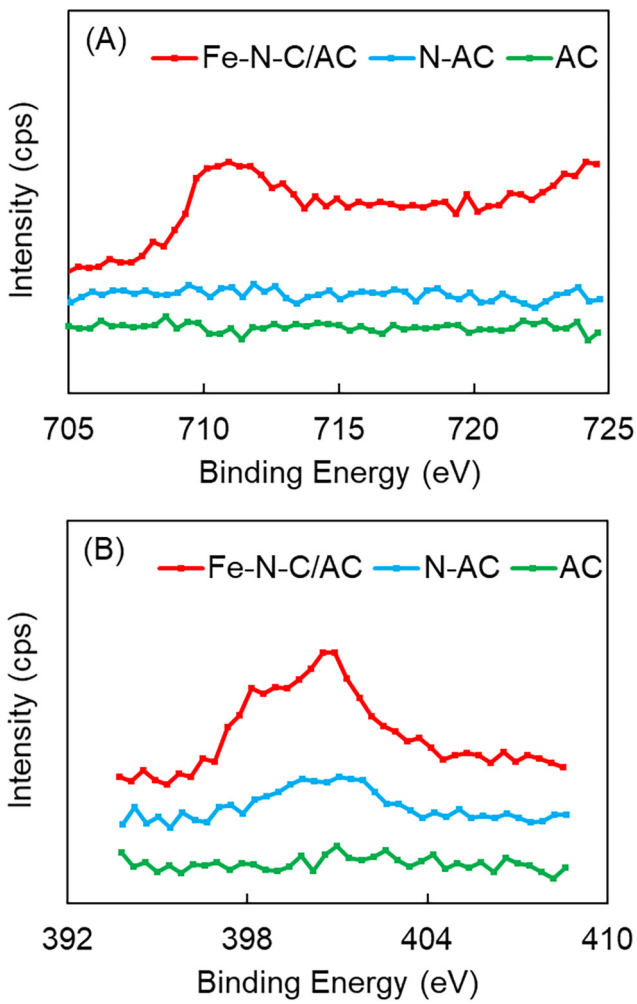

Fig. 3. XPS spectra of AC, N–AC, and Fe–N–C/AC catalysts at the (A) Fe2p peak and (B) N1s peak.

Table 1
Elemental compositions of AC, N–AC and Fe–N–C/AC catalysts.

Catalyst	C (%)	O (%)	N (%)	Fe (%)
AC	96.6	3.3	0.1	–
N–AC	97.7	1.5	0.8	–
Fe–N–C/AC	93.3	3.5	2.5	0.7

IN; +0.209 V vs a standard hydrogen electrode) was placed close to the anode brush within the current path between anode and cathode, to measure the anode potentials ($E_{An,m}$). The anode potentials (E_{An}) and cathode potentials (E_{Cat}) were then calculated and corrected based on the solution conductivity and electrode distances from the reference electrode from the following equations [35]:

$$\frac{R_\Omega}{l} = \frac{10^3}{\sigma A} \tag{1}$$

$$E_{An} = E_{An,m} - \left(\frac{10^3 R_\Omega d_{An-RE}}{l}\right) i \tag{2}$$

$$E_{Cat} = (E_{An} + U) + \left(\frac{10^3 R_\Omega d_{Cat-RE}}{l}\right) i \tag{3}$$

where R_Ω/l is the solution ohmic resistance per distance ($\Omega\,cm^{-1}$), d_{An-Cat} is the distance between anode and cathode (1 cm), σ is the solution conductivity measured for 50 mM PBS ($mS\,cm^{-1}$), A is the electrode projected area (cm^2), d_{An-RE} and d_{Cat-RE} are the distances from the anode or cathode to the reference electrode (cm). All potentials are reported here versus SHE. The measured electrode potentials (not corrected for solution resistance) are also reported in Fig. S1.

2.5. Electrode potential slope analysis

An electrode potential slope (EPS) analysis was used to evaluate the area based resistance and working potentials of the anodes and cathodes [36]. The linear region of the cathode or anode polarization curves at current densities near the maximum power density (typically 3–9 $A\,m^{-2}$ in 50 mM PBS) was fitted with $E = ai + b$, where E is the electrode potential (mV), i is the current density ($A\,m^{-2}$), a is the slope and b is the y-intercept. The electrode specific resistance ($R_{An,s}$ or $R_{Cat,s}$, $m\Omega\,m^2$) was then equal to the magnitude of the slope, and the experimental open circuit half-cell potential ($E_{An,e0}$ or $E_{Cat,e0}$, mV) was the y-intercept. The calculated electrode specific resistance and experimental open circuit half-cell potential are independent of non-electrode variables such as media type or reactor configuration, therefore enabling valid evaluation of the electrode performance and cross-study comparisons. As EPS analysis only used of the linear region of the electrode polarization curves, a simulated power density curve was generated to verify a valid fitting of the full polarization data, using:

$$R_\Omega = \frac{10^3 d_{An-RE}}{\sigma A} \tag{4}$$

$$R_{Cat} = \frac{10 R_{Cat,s}}{A} \tag{5}$$

$$R_{An} = \frac{10 R_{An,s}}{A} \tag{6}$$

$$E_{emf,e0} = E_{cat,e0} - E_{An,e0} \tag{7}$$

$$P = \frac{{E_{emf,e0}}^2}{10^2 (R_\Omega + R_{Cat} + R_{An}) A} \tag{8}$$

where R_Ω is the solution resistance (Ω), R_{Cat} is the cathode resistance (Ω), R_{An} is the anode resistance (Ω), $E_{emf,e0}$ is the experimental electromotive force (mV), P is the power density ($W\,m^{-2}$).

2.6. Electrochemical analysis

The electrochemical performance of the fabricated cathodes were characterized using linear sweep voltammetry (LSV) in an abiotic electrochemical cell containing two chambers (each 2 cm in length, 3 cm in diameter) separated by an anion exchange membrane (AEM; AMI-7001, Membrane International Inc., USA). Platinum mesh (1 cm by 2 cm) was used as the counter electrode. An Ag/AgCl reference electrode was placed close to the cathode and kept in the same position for all tests. The electrolyte was 50 mM PBS prepared as described above. All potentials were reported versus a standard hydrogen electrode (SHE). A multichannel potentiostat (VMP3 Multichannel Workstation, Biologic Science Instruments, USA) was used to conduct the electrochemical tests in a constant temperature room (30 °C). The potentials on the cathodes were scanned from +0.509 V to −0.209 V (vs. SHE) at a scan rate of 0.1 $mV\,s^{-1}$ for 7 times to reach steady conditions, and plotted with data from the seventh scan.

A rotating disk electrode (RDE) was used to evaluate the catalytic activity in the absence of mass transfer limitation [37]. To prepare the catalyst ink, 30 mg of prepared catalyst material (Fe–N–C/AC, N–AC or AC) was added into 3 mL of dimethylformamide (Sigma Aldrich, USA) and sonicated (Model 450, Branson, USA) at 20% power for 8 min in an ice bath. Then, 270 μL of Nafion (5 wt%, Sigma Aldrich, USA) was added into the solution and sonicated for another 8 min. After sonication, 10 μL of the ink solution was drop coated onto a glassy carbon electrode (Pine Instruments, USA) with a diameter of 5 mm, and dried

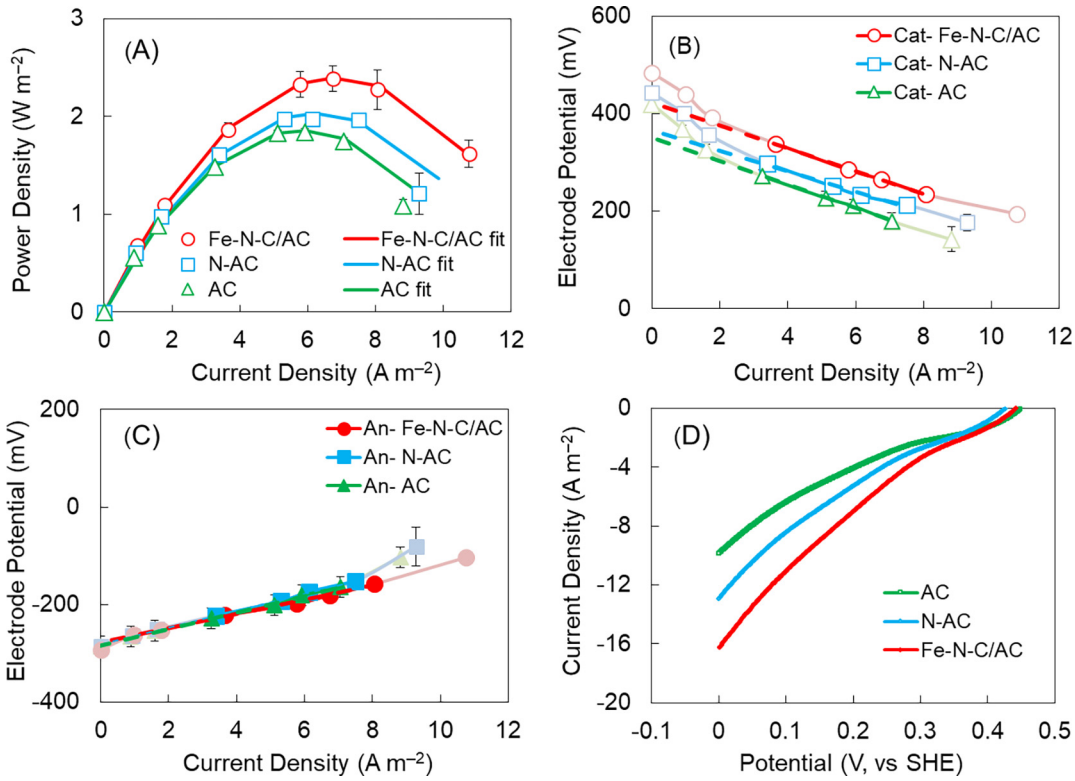

Fig. 4. (A) Measured (marked points) and modeled (solid lines) power density curves in 50 mM PBS for AC, N–AC and Fe–N–C/AC cathodes. (B, C) Cathode and anode potentials in 50 mM PBS with corrected solution resistance (The dashed lines represent the data that would be obtained from polarization tests, while the thick solid lines show the linearized portion of the slopes that are used to calculate the anode (R_{An}) and cathode (R_{Cat}) resistances). (D) LSV curves for AC, N–AC and Fe–N–C/AC cathodes in an electrochemical cell.

overnight in a fumehood. All RDE tests were conducted in 50 mM PBS under both nitrogen and then air ambient condition at a constant temperature room (30 °C). The solutions were first sparged with nitrogen for 30 min before conducting linear sweep voltammetry tests, and nitrogen gas was constantly flowed into the headspace during LSV runs. The electrical potential of the disk electrode was scanned from 0.2 V to −1 V (vs. Ag/AgCl) at 10 mV s^{-1}, at rotation rates from 100 rpm to 2100 rpm. Then, the test was repeated following the same procedure but with air sparging, and the current generated under nitrogen sparging was subtracted from that obtained under air sparging to evaluate current generation due only to oxygen reduction [17].

The electron-transfer number (n) for the ORR was calculated from the RDE data using the Koutecky–Levich equation [17]:

$$\frac{1}{i} = \frac{1}{i_k} - \frac{1}{0.620nFA_d D^{2/3} c\nu^{-1/6}\omega^{1/2}} \quad (4)$$

where i is the measured reduction current, i_k is the kinetic current, n is the number of electrons transferred in the reaction, F is the Faraday constant, A_d is the geometric surface area of the disk electrode, D is the oxygen diffusion coefficient, c is the concentration of oxygen in the solution, ν is the kinematic viscosity, and ω is the rotation rate of the electrode [38].

3. Results and discussions

3.1. Catalyst structure and surface properties

Direct pyrolysis of the preformed Fe(III)-chitosan hydrogel generated a more uniformly porous structure on Fe–N–C/AC catalyst surface compared to that of N–AC or AC. The AC without any treatment and N–AC with only chitosan addition both showed a solid and dense surface morphology (Fig. 2A and 2B), suggesting pyrolysis of additional chitosan did not significantly alter the surface morphology of the AC support. As chitosan itself is not soluble in water without forming chelates, the added chitosan could directly undergo carbonization and form a carbonaceous structure that is similar to AC without appreciable morphology changes [39]. However, the preformation of Fe(III)-chitosan hydrogel produced a Fe–N_x scaffold on the AC support during drying step, with a relatively uniform and porous structure (Fig. 2C). A uniform distribution of Fe on the Fe–N–C/AC catalyst surface without any significant agglomeration was observed based on EDS mapping (Fig. 2D), which could potentially make more catalytic sites accessible for ORR and thereby improve the overall catalytic performance. In addition, the Fe–N–C/AC catalyst showed the highest BET surface area of 760 $m^2 g^{-1}$ compared to N–AC (650 $m^2 g^{-1}$) and AC (580 $m^2 g^{-1}$), demonstrating the formation of a more porous structure by using the Fe (III)-chitosan hydrogel (Fig. S2). A high surface area was beneficial for the oxygen reduction due to more accessible active sites as previously demonstrated [40].

The formation of the Fe–N–C catalyst on the AC surface was identified from the Fe and N peaks based on XPS spectra. A significant Fe peak was observed for Fe–N–C/AC catalyst near 710.8 eV, which was attributed to the Fe(III) peak [41], and peak fitting indicated an iron content of ~0.7% (Fig. 3A, Table 1). No Fe peak was detected for the AC and N–AC samples (Fig. 3A). The slight shift of the Fe peak away from 710.8 eV towards high binding energy might have resulted from the electron negative environment around Fe due to the existence of oxygen or nitrogen containing functional groups [42]. The highest nitrogen content of 2.5% was obtained for the Fe–N–C/AC catalyst, followed by 0.8% for N–AC and 0.1% for AC based on the N1s peak fitting (Fig. 3B, Table 1). The N peak at 399.0 eV for Fe–N–C/AC catalyst corresponded well to Fe–N bonding as reported in a previous study [43], demonstrating the formation of Fe–N–C catalyst. The N–AC had lower nitrogen content compared to Fe–N–C/AC, even with the same amount of chitosan addition, which indicated that the nitrogen doping

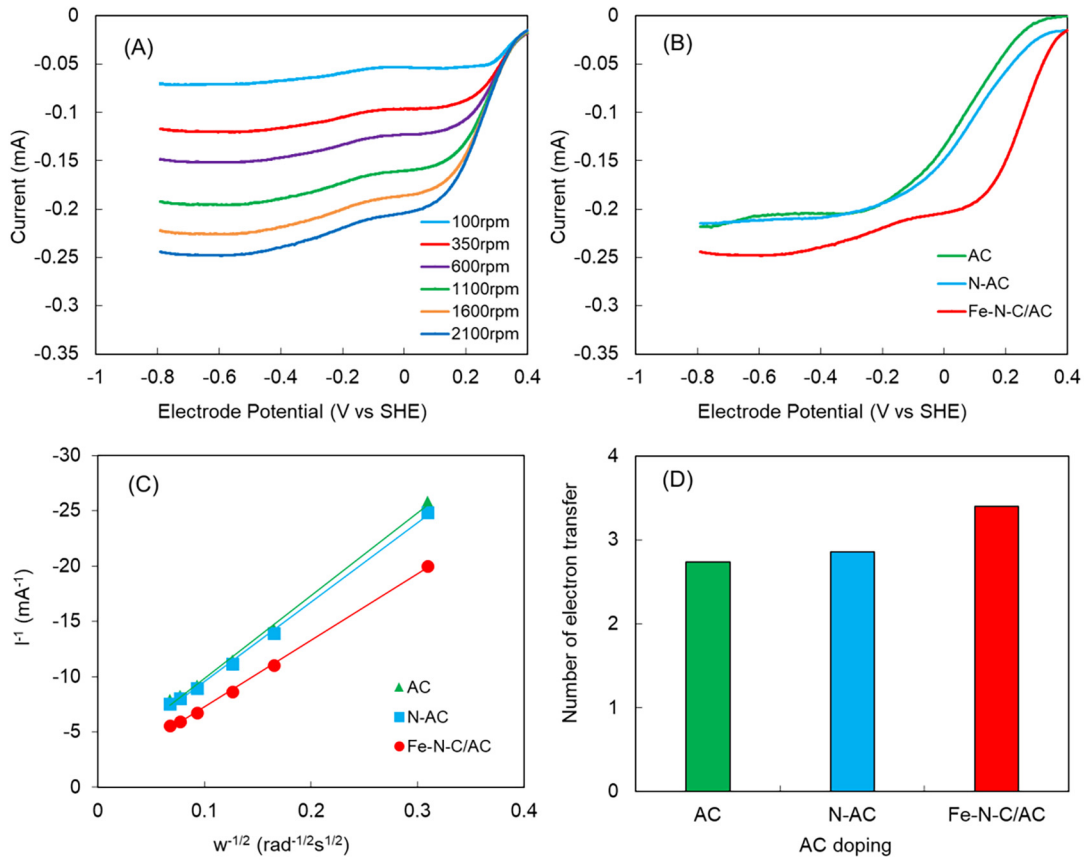

Fig. 5. (A) LSV curves for Fe–N–C/AC catalyst in 50 mM PBS at different rotation speed in RDE testing. (B) LSV curves for AC, N–AC, and Fe–N–C/AC catalysts in 50 mM at 2100 rpm. (C) Koutecky–Levich plots of different catalysts at 0 V vs. SHE. (D) Electron–transfer number for different catalysts at 0 V vs. SHE.

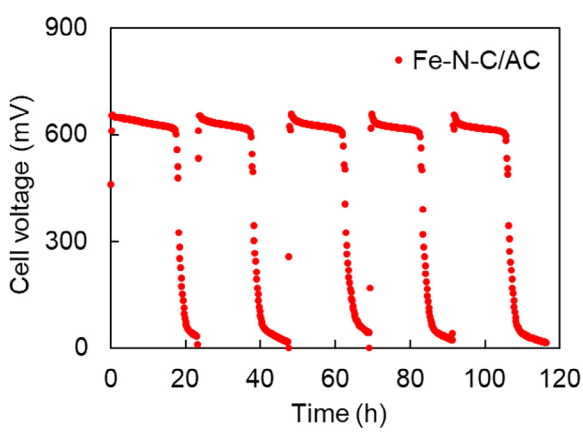

Fig. 6. Voltage curve of Fe–N–C/AC cathode operated in MFC for 120 h at an external resistance of 1000 Ω.

efficiency was greatly increased as a result of the Fe(III)-chitosan chelates formation. The XRD analysis also showed the main phases of Fe on Fe–N–C/AC catalyst surfaces are Fe_3O_4 (diffraction peak at 35°, 04-012-7038) and Fe–N_x (diffraction peaks at 41°, 04-012-3036 and 43°, 01-073-2103) (Fig. S3), indicating the formation of Fe–N–C catalyst. The formation of Fe–N_x was critical for catalyzing oxygen reduction in four electron transfer pathway as demonstrated in previous studies [40,44,45].

3.2. Cathode performance in MFCs and electrochemical cells

The highest maximum power density was obtained from the MFCs with Fe–N–C/AC cathodes, showing a maximum power density of 2.4 ± 0.1 W m^{-2}. This power density was 33% higher than that produced by the AC cathodes with a maximum power density of 1.8 ± 0.03 W m^{-2}, and also 20% higher than 2.0 ± 0.07 W m^{-2} from N–AC cathodes (Fig. 4A). The power density of 1.8 ± 0.03 W m^{-2} obtained for the plain AC cathode here was higher than those previously reported for cathodes using AC catalyst with an average power density of 1.4 ± 0.1 W m^{-2} [2], indicating higher than typical performance of the control cathodes but still an appreciable improvement in power production with the newly prepared cathodes.

The use of the Fe–N–C catalyst on AC significantly boosted the $E_{Cat,e0}$ (experimental open circuit half-cell potential for cathode) to 424 ± 4 mV, which was 16% higher than 366 ± 11 mV for N–AC cathodes and 21% higher than 350 ± 4 mV for AC cathodes (Fig. 4B). The similar $E_{Cat,e0}$ observed for the N–AC and AC cathodes suggested a similar catalytic pathway (2 e^- transfer), while the significant increase of $E_{Cat,e0}$ for Fe–N–C/AC cathodes demonstrated a change of catalytic pathway to be more efficient towards ORR (4 e^- transfer). The $R_{Cat,s}$ (cathode specific resistance) for Fe–N–C/AC (24 ± 1 mΩ m^2), N–AC (21 ± 2 mΩ m^2) and AC (24 ± 1 mΩ m^2) cathodes were similar (Fig. 4B), which could possibly result from similar cathode structures. The difference in power production mainly resulted from the differences in performance of the catalysts in the cathodes, as the anode performance remained similar for all MFC reactors in terms of both $E_{An,e0}$ (experimental open circuit half-cell potential for anode, −282 ± 4 mV on average) and $R_{An,s}$ (anode specific resistance, 16 ± 1 mΩ m^2 on average) (Fig. 4C, Table S1).

The Fe–N–C/AC cathodes also showed the best electrochemical performance compared to N–AC and AC cathodes in LSV tests over a wider potential window than that examined using MFCs (Fig. 4D). For instance, at 0 V versus SHE, the Fe–N–C/AC cathode showed a maximum current density of 16.2 A m^{-2}, which was larger than 12.9 A m^{-2}

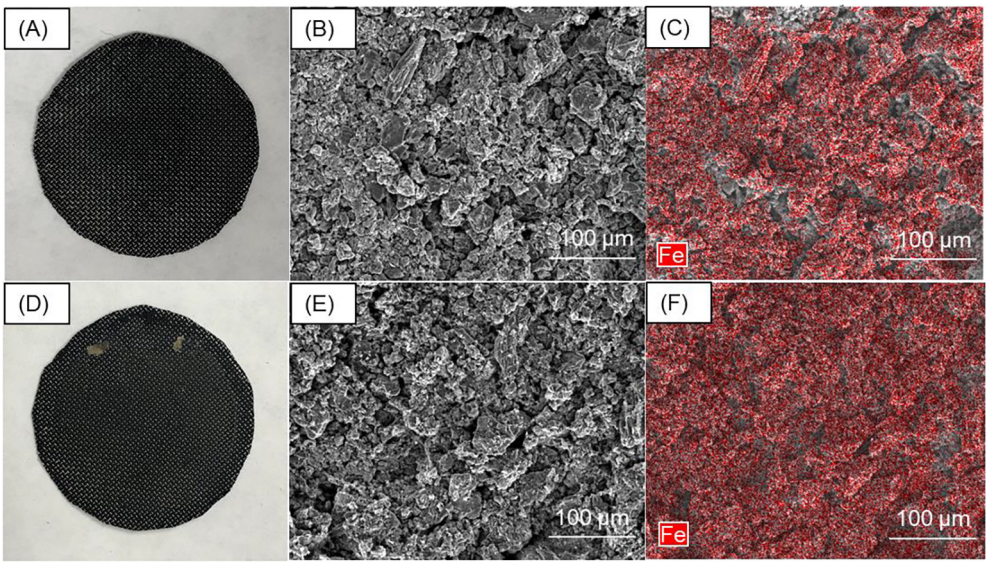

Fig. 7. (A) Image of Fe–N–C/AC cathode, (B) SEM of cathode surface, (C) EDS mapping of Fe on cathode surface before operation in MFC. (D) Image of Fe–N–C/AC cathode, (E) SEM of cathode surface, (F) EDS mapping of Fe on cathode surface after operation in MFC for 120 h.

for N–AC cathode and 9.8 A m^{-2} for AC cathode, indicating the highest reactivity from the Fe–N–C/AC cathode. At a more positive potential of 0.2 V versus SHE, the Fe–N–C/AC cathode still had a current density of 7 A m^{-2}, which was 35% larger than 5.2 A m^{-2} for N–AC cathode and 75% larger than 4 A m^{-2} for AC cathode (Fig. 4D).

3.3. ORR characterization of synthesized catalysts

By minimizing mass transfer limitations using RDE tests, the Fe–N–C/AC catalyst produced the highest limiting current compared to N–AC and AC catalysts. At the potential of −0.8 V versus SHE at 2100 rpm where current stabilized, the Fe–N–C/AC catalyst had a current of 0.25 mA, which was 19% higher than 0.21 mA for N–AC and AC catalysts (Fig. 5A and 5B), suggesting a higher ORR activity from Fe–N–C/AC catalyst. The Fe–N–C/AC catalyst also showed an earlier half-wave potential of 0.25 V, which was 1.5 times more positive than 0.10 V for N–AC catalyst and 2.6 times more positive than 0.07 V for AC catalyst (Fig. 5B), indicating less over-potential in catalyzing ORR for Fe–N–C/AC catalyst.

Based on Koutecky-Levich fitting, the Fe–N–C/AC catalyst showed a nearly four electron transfer pathway towards ORR with an electron transfer number of 3.4, which was higher than 2.7 for AC catalyst and 2.8 for N–AC catalyst (Fig. 5C and 5D). The increase in the electron transfer number for Fe–N–C/AC catalyst was attributed to the incorporation of the highly active Fe–N–C catalytic sites as previously proved to be a perfect four electron transfer reaction towards ORR [43]. The N–AC catalysts still behaved as a two electron transfer catalyst, which was probably due to the small amount of chitosan addition and thus low nitrogen doping with no significant increase in ORR activity. It was also previously demonstrated that doping Fe on AC alone did not impact the catalytic performance of AC, demonstrating the importance of Fe and N co-doping [20]. Therefore, the formation of Fe–N–C catalyst on AC from Fe(III)–chitosan hydrogel was more efficient in boosting the ORR reactivity compared to solely nitrogen doping using chitosan.

3.4. Fe–N–C/AC cathode stability

The Fe–N–C/AC cathode showed good stability over 120 h operation in MFCs. The voltage generation of the MFC with the Fe–N–C/AC cathode stabilized at ~630 mV over repeated cycles (Fig. 6). No decrease or change in the cycles of voltage generation over 120 h indicated that the Fe–N–C/AC catalyst maintained the initial oxygen catalytic reactivity after use. Surface characterization was conducted on the Fe–N–C/AC cathode before and after these tests to further examine the cathode stability. After operation in the MFC for 120 h, there was no observable change in the surface properties of the Fe–N–C/AC cathode except for the development of a thin cathodic biofilm (Fig. 7A and 7D), which is commonly observed in single chamber MFCs [46]. No surface morphology change on the Fe–N–C/AC cathode was observed under SEM before and after usage (Fig. 7B and 7E). Fe was clearly identified on the Fe–N–C/AC cathode surface after usage (Fig. 7F), which was similar to that on initial Fe–N–C/AC cathode before use (Fig. 7C). The well-maintained cathode structure and existence of Fe on Fe–N–C/AC cathode surface after usage based on SEM and EDX mapping demonstrated the good stability of Fe–N–C/AC cathode.

3.5. Cost-performance analysis

The maximum power density of 2.4 ± 0.1 W m^{-2} from the Fe–N–C/AC cathodes was among the top high power densities achieved in MFCs with same reactor configuration and solution conditions. This maximum power density was also higher than other modification methods such as nitrogen doping, metal oxide blending, or bimetallic catalysts addition, which generated power densities from 1.6 to 1.9 W m^{-2} [47–51]. Compared to the state-of-art power density of 2.6 W m^{-2} previously obtained with catalysts derived from iron-phenanthroline complexes [20], the 2.4 ± 0.1 W m^{-2} achieved in this study is slightly lower but the use of chitosan was a more sustainable approach.

Most of the cost in synthesizing Fe–N–C catalysts resulted from the use of nitrogen containing precursors because iron salts such as $FeCl_3$ are only \$0.3 kg^{-1}. Here, chitosan was by far the cheapest N containing precursor for the synthesis of Fe–N–C catalyst, with a low price of ~ \$25 kg^{-1} (Table S3). Based on the material loading for cathode fabrication, the material cost for synthesizing the Fe–N–C catalyst from $FeCl_3$ and chitosan was only \$2.2 m^{-2}, which was only 6% of the estimated overall materials costs for fabricating the plain activated carbon cathode (\$36 m^{-2}). With only this 6% increase in material cost, the maximum power density of MFCs increased by 33% using the Fe–N–C/AC catalyst. Therefore, using chitosan for synthesizing Fe–N–C catalyst was an economically viable approach to enhance the power production in MFCs.

4. Conclusions

The Fe–N–C catalyst on AC support was successfully synthesized from ferric chloride and chitosan precursors, as identified by the clear Fe and N peaks from the XPS spectra. The preformed Fe(III)-chitosan hydrogel as a supporting scaffold generated a porous structure on AC during pyrolysis with uniform distribution of Fe active sites based on EDS mapping. A maximum power density of $2.4 \pm 0.1\,W\,m^{-2}$ was obtained in MFCs using Fe–N–C/AC catalyst, and it was 33% higher than $1.8 \pm 0.03\,W\,m^{-2}$ for the control MFCs using a plain AC catalyst. The synthesized Fe–N–C/AC catalyst had a larger electron transfer number of 3.4 than 2.6 for AC and 2.7 for N–AC, indicating the improved ORR activity and transition from a two electron transfer pathway to a four electron transfer pathway towards ORR for the Fe–N–C/AC catalyst. Using chitosan as the N containing precursor and ferric chloride for Fe–N–C synthesis added 6% more in material cost for cathode fabrication, but it produced a 33% increase in the maximum power density, demonstrating an economically viable approach to enhance power production in MFCs owing to the low cost and wide availability of chitosan.

Acknowledgements

This research was supported by the King Abdullah University of Science and Technology (KAUST) (OSR-2017-CPF-2907-02), and Penn State University.

Appendix A. Supplementary data

Supplementary data to this article can be found online at https://doi.org/10.1016/j.cej.2019.122522.

References

[1] B.E. Logan, P. Aelterman, B. Hamelers, R. Rozendal, U. Schröder, J. Keller, S. Freguiac, W. Verstraete, K. Rabaey, Microbial fuel cells: methodology and technology, Environ. Sci. Technol. 40 (2006) 5181–5192.
[2] W. Yang, K.-Y. Kim, P.E. Saikaly, B.E. Logan, The impact of new cathode materials relative to baseline performance of microbial fuel cells all with the same architecture and solution chemistry, Energy Environ. Sci. 10 (2017) 1025–1033.
[3] S. Lu, H. Li, G. Tan, F. Wen, M.T. Flynn, X. Zhu, Resource recovery microbial fuel cells for urine-containing wastewater treatment without external energy consumption, Chem. Eng. J. (2019).
[4] F. Xu, F.-Q. Cao, Q. Kong, L.-L. Zhou, Q. Yuan, Y.-J. Zhu, Q. Wang, Electricity production and evolution of microbial community in the constructed wetland-microbial fuel cell, Chem. Eng. J. 339 (2018) 479–486.
[5] H. Zhao, C.-H. Kong, Enhanced removal of p-nitrophenol in a microbial fuel cell after long-term operation and the catabolic versatility of its microbial community, Chem. Eng. J. 339 (2018) 424–431.
[6] X. Song, Q. Jiang, J. Liu, Y. Shao, Y. Feng, Enhanced electricity generation and water pressure tolerance using carbon black-based sintered filtration air-cathodes in microbial fuel cells, Chem. Eng. J. 369 (2019) 652–659.
[7] D.R. Lovley, Bug juice: harvesting electricity with microorganisms, Nat. Rev. Microbiol. 4 (2006) 497–508.
[8] B.E. Logan, Microbial Fuel Cells, John Wiley & Sons Inc, Hoboken, NJ, 2008.
[9] X. Ying, D. Shen, M. Wang, H. Feng, Y. Gu, W. Chen, Titanium dioxide thin film-modified stainless steel mesh for enhanced current-generation in microbial fuel cells, Chem. Eng. J. 333 (2018) 260–267.
[10] X. Zhang, X. Miao, J. Li, Z. Li, Evaluation of electricity production from Fenton oxidation pretreated sludge using a two-chamber microbial fuel cell, Chem. Eng. J. 361 (2019) 599–608.
[11] F. Zhang, S. Cheng, D. Pant, G.V. Bogaert, B.E. Logan, Power generation using an activated carbon and metal mesh cathode in a microbial fuel cell, Electrochem. Commun. 11 (2009) 2177–2179.
[12] S.A. Cheng, J.C. Wu, Air-cathode preparation with activated carbon as catalyst, PTFE as binder and nickel foam as current collector for microbial fuel cells, Bioelectrochemistry 92 (2013) 22–26.
[13] Y. Park, S. Park, V.K. Nguyen, J. Yu, C.I. Torres, B.E. Rittmann, T. Lee, Complete nitrogen removal by simultaneous nitrification and denitrification in flat-panel air-cathode microbial fuel cells treating domestic wastewater, Chem. Eng. J. 316 (2017) 673–679.
[14] N. Yang, G. Zhan, D. Li, X. Wang, X. He, H. Liu, Complete nitrogen removal and electricity production in Thauera-dominated air-cathode single chambered microbial fuel cell, Chem. Eng. J. 356 (2019) 506–515.
[15] X. Tian, M. Zhou, C. Tan, M. Li, L. Liang, K. Li, P. Su, KOH activated N-doped novel carbon aerogel as efficient metal-free oxygen reduction catalyst for microbial fuel cells, Chem. Eng. J. 348 (2018) 775–785.
[16] W. Yang, W. He, F. Zhang, M.A. Hickner, B.E. Logan, Single step fabrication using a phase inversion method of poly (vinylidene fluoride)(PVDF) activated carbon air cathodes for microbial fuel cells, Environ. Sci. Technol. Lett. 1 (2014) 416–420.
[17] V.J. Watson, C. Nieto Delgado, B.E. Logan, Influence of chemical and physical properties of activated carbon powders on oxygen reduction and microbial fuel cell performance, Environ. Sci. Technol. 47 (2013) 6704–6710.
[18] F. Jaouen, V. Goellner, M. Lefevre, J. Herranz, E. Proietti, J.P. Dodelet, Oxygen reduction activities compared in rotating-disk electrode and proton exchange membrane fuel cells for highly active Fe-N-C catalysts, Electrochim. Acta 87 (2013) 619–628.
[19] C. Santoro, A. Serov, R. Gokhale, S. Rojas-Carbonell, L. Stariha, J. Gordon, K. Artyushkova, P. Atanassov, A family of Fe-NC oxygen reduction electrocatalysts for microbial fuel cell (MFC) application: relationships between surface chemistry and performances, Appl. Catal. B 205 (2017) 24–33.
[20] W. Yang, B.E. Logan, Immobilization of a metal–nitrogen–carbon catalyst on activated carbon with enhanced cathode performance in microbial fuel cells, ChemSusChem 9 (2016) 2226–2232.
[21] H. Tang, Y. Zeng, Y. Zeng, R. Wang, S. Cai, C. Liao, H. Cai, X. Lu, P. Tsiakaras, Iron-embedded nitrogen doped carbon frameworks as robust catalyst for oxygen reduction reaction in microbial fuel cells, Appl. Catal. B 202 (2017) 550–556.
[22] B.E. Logan, M.J. Wallack, K.-Y. Kim, W. He, Y. Feng, P.E. Saikaly, Assessment of microbial fuel cell configurations and power densities, Environ. Sci. Technol. Lett. 2 (2015) 206–214.
[23] J. Ma, Y. Sahai, Chitosan biopolymer for fuel cell applications, Carbohydr. Polym. 92 (2013) 955–975.
[24] M. Rinaudo, Chitin and chitosan: properties and applications, Prog. Polym. Sci. 31 (2006) 603–632.
[25] W.L. Yan, R. Bai, Adsorption of lead and humic acid on chitosan hydrogel beads, Water Res. 39 (2005) 688–698.
[26] S. Mekahlia, B. Bouzid, Chitosan-Copper (II) complex as antibacterial agent: synthesis, characterization and coordinating bond-activity correlation study, Phys. Procedia 2 (2009) 1045–1053.
[27] C. Shen, H. Chen, S. Wu, Y. Wen, L. Li, Z. Jiang, M. Li, W. Liu, Highly efficient detoxification of Cr (VI) by chitosan–Fe (III) complex: process and mechanism studies, J. Hazard. Mater. 244 (2013) 689–697.
[28] B. Liang, K. Li, Y. Liu, X. Kang, Nitrogen and phosphorus dual-doped carbon derived from chitosan: An excellent cathode catalyst in microbial fuel cell, Chem. Eng. J. 358 (2019) 1002–1011.
[29] W. Yang, B.E. Logan, Engineering a membrane based air cathode for microbial fuel cells via hot pressing and using multi-catalyst layer stacking, Environ. Sci. Water Res. Technol. 2 (2016) 858–863.
[30] J. Rouquerol, D. Avnir, C. Fairbridge, D. Everett, J. Haynes, N. Pernicone, J. Ramsay, K. Sing, K. Unger, Recommendations for the characterization of porous solids (Technical Report), Pure Appl. Chem. 66 (1994) 1739–1758.
[31] B.E. Logan, S. Cheng, V. Watson, G. Estadt, Graphite fiber brush anodes for increased power production in air-cathode microbial fuel cells, Environ. Sci. Technol. 41 (2007) 3341–3346.
[32] S. Cheng, D. Xing, D.F. Call, B.E. Logan, Direct biological conversion of electrons into methane by electromethanogenesis, Environ. Sci. Technol. 43 (2009) 3953–3958.
[33] S. Cheng, D. Xing, D.F. Call, B.E. Logan, Direct biological conversion of electrical current into methane by electromethanogenesis, Environ. Sci. Technol. 43 (2009) 3953–3958.
[34] W. Yang, K.-Y. Kim, B.E. Logan, Development of carbon free diffusion layer for activated carbon air cathode of microbial fuel cells, Biores. Technol. 197 (2015) 318–322.
[35] B.E. Logan, E. Zikmund, W. Yang, R. Rossi, K.-Y. Kim, P.E. Saikaly, F. Zhang, Impact of ohmic resistance on measured electrode potentials and maximum power production in microbial fuel cells, Environ. Sci. Technol. 52 (2018) 8977–8985.
[36] R. Rossi, B.P. Cario, C. Santoro, W. Yang, P.E. Saikaly, B.E. Logan, Evaluation of electrode and solution area-based resistances enables quantitative comparisons of factors impacting microbial fuel cell performance, Environ. Sci. Technol. 53 (2019) 3977–3986.
[37] W. Yang, V.J. Watson, B.E. Logan, Substantial humic acid adsorption to activated carbon air cathodes produces a small reduction in catalytic activity, Environ. Sci. Technol. 50 (2016) 8904–8909.
[38] Y. Chen, Z. Lv, J. Xu, D. Peng, Y. Liu, J. Chen, X. Sun, C. Feng, C. Wei, Stainless steel mesh coated with MnO 2/carbon nanotube and polymethylphenyl siloxane as low-cost and high-performance microbial fuel cell cathode materials, J. Power Sources 201 (2012) 136–141.
[39] Y. Liu, Y. Zhao, K. Li, Z. Wang, P. Tian, D. Liu, T. Yang, J. Wang, Activated carbon derived from chitosan as air cathode catalyst for high performance in microbial fuel cells, J. Power Sources 378 (2018) 1–9.
[40] D. Lyu, Y.B. Mollamahale, S. Huang, P. Zhu, X. Zhang, Y. Du, S. Wang, M. Qing, Z.Q. Tian, P.K. Shen, Ultra-high surface area graphitic Fe-NC nanospheres with single-atom iron sites as highly efficient non-precious metal bifunctional catalysts towards oxygen redox reactions, J. Catal. 368 (2018) 279–290.
[41] M.C. Biesinger, B.P. Payne, A.P. Grosvenor, L.W. Lau, A.R. Gerson, R.S.C. Smart, Resolving surface chemical states in XPS analysis of first row transition metals, oxides and hydroxides: Cr, Mn, Fe, Co and Ni, Appl. Surf. Sci. 257 (2011) 2717–2730.
[42] S. Rojas-Carbonell, K. Artyushkova, A. Serov, C. Santoro, I. Matanovic, P. Atanassov, Effect of pH on the activity of platinum group metal-free catalysts in oxygen reduction reaction, ACS Catal. 8 (2018) 3041–3053.

[43] K. Yuan, S. Sfaelou, M. Qiu, D. Lützenkirchen-Hecht, X. Zhuang, Y. Chen, C. Yuan, X. Feng, U. Scherf, Synergetic contribution of boron and Fe–N x species in porous carbons toward efficient electrocatalysts for oxygen reduction reaction, ACS Energy Lett. 3 (2017) 252–260.
[44] Y. Dai, Y. Chan, B. Jiang, L. Wang, J. Zou, K. Pan, H. Fu, Bifunctional Ag/Fe/N/C catalysts for enhancing oxygen reduction via cathodic biofilm inhibition in microbial fuel cells, ACS Appl. Mater. Interfaces 8 (2016) 6992–7002.
[45] Y. Liu, Y.-S. Fan, Z.-M. Liu, Pyrolysis of iron phthalocyanine on activated carbon as highly efficient non-noble metal oxygen reduction catalyst in microbial fuel cells, Chem. Eng. J. 361 (2019) 416–427.
[46] W. Yang, R. Rossi, Y. Tian, K.-Y. Kim, B.E. Logan, Mitigating external and internal cathode fouling using a polymer bonded separator in microbial fuel cells, Biores. Technol. 249 (2018) 1080–1084.
[47] P. Zhang, K. Li, X. Liu, Carnation-like MnO2 modified activated carbon air cathode improve power generation in microbial fuel cells, J. Power Sources 264 (2014) 248–253.
[48] X. Xia, F. Zhang, X. Zhang, P. Liang, X. Huang, B.E. Logan, Use of pyrolyzed Iron ethylenediaminetetraacetic acid modified activated carbon as air–cathode catalyst in microbial fuel cells, ACS Appl. Mater. Interfaces 5 (2013) 7862–7866.
[49] X. Guo, J. Jia, H. Dong, Q. Wang, T. Xu, B. Fu, R. Ran, P. Liang, X. Huang, X. Zhang, Hydrothermal synthesis of FeMn bimetallic nanocatalysts as high-efficiency cathode catalysts for microbial fuel cells, J. Power Sources 414 (2019) 444–452.
[50] Q. Huang, P. Zhou, H. Yang, L. Zhu, H. Wu, In situ generation of inverse spinel CoFe2O4 nanoparticles onto nitrogen-doped activated carbon for an effective cathode electrocatalyst of microbial fuel cells, Chem. Eng. J. 325 (2017) 466–473.
[51] X. Xia, M. Li, T. Liu, P. Liang, X. Huang, Facile synthesis of cobalt oxide as electrocatalyst for the oxygen reduction reaction in microbial fuel cells, Chem. Eng. J. 342 (2018) 395–400.